Check for updates

Effect of crystallite geometries on electrochemical performance of porous intercalation electrodes by multiscale operando investigation

Yuting Luo[1,2], Yang Bai[3], Aashutosh Mistry [4], Yuwei Zhang[5], Dexin Zhao[2], Susmita Sarkar [6], Joseph V. Handy[1,2], Shahed Rezaei[3], Andrew Chihpin Chuang [7], Luis Carrillo[1,2], Kamila Wiaderek[7], Matt Pharr [5], Kelvin Xie[2], Partha P. Mukherjee [6 ✉], Bai-Xiang Xu[3 ✉] and Sarbajit Banerjee [1,2 ✉]

Lithium-ion batteries are yet to realize their full promise because of challenges in the design and construction of electrode architectures that allow for their entire interior volumes to be reversibly accessible for ion storage. Electrodes constructed from the same material and with the same specifications, which differ only in terms of dimensions and geometries of the constituent particles, can show surprising differences in polarization, stress accumulation and capacity fade. Here, using operando synchrotron X-ray diffraction and energy dispersive X-ray diffraction (EDXRD), we probe the mechanistic origins of the remarkable particle geometry-dependent modification of lithiation-induced phase transformations in V_2O_5 as a model phase-transforming cathode. A pronounced modulation of phase coexistence regimes is observed as a function of particle geometry. Specifically, a metastable phase is stabilized for nanometre-sized spherical V_2O_5 particles, to circumvent the formation of large misfit strains. Spatially resolved EDXRD measurements demonstrate that particle geometries strongly modify the tortuosity of the porous cathode architecture. Greater ion-transport limitations in electrode architectures comprising micrometre-sized platelets result in considerable lithiation heterogeneities across the thickness of the electrode. These insights establish particle geometry-dependent modification of metastable phase regimes and electrode tortuosity as key design principles for realizing the promise of intercalation cathodes.

Several decades after the advent of intercalation batteries[1–5], the theoretical capacity of cathode materials remains to be realized in full measure, largely because of challenges in the design and construction of porous electrode architectures that allow for the entirety of their interior volumes to be reversibly accessible for ion storage[6]. In insertion cathodes, the spatiotemporal dynamics of ions inserted within each particle are determined by redox events at the interfaces, as governed by local electrochemical potentials[7–11]. Such processes show a strong dependence on particle dimensions and geometries, the nature of the interfaces and the relative positioning of the particle within the electrode architecture[12–14]. The electrode response is the cumulative response of a distribution of interconnected individual particles, and manifests considerable heterogeneity across length scales[8,15–18]. In this article, we seek to explain the surprising differences in polarization, stress accumulation and capacity fade observed even at low intercalation rates for porous electrode architectures constructed to the same specifications, which vary only in terms of the particle geometry of the constituent particles for V_2O_5, a model phase-transforming cathode.

Layered α-V_2O_5 is a model phase-transforming cathode material as a result of its interlayer sites for accommodating Li-ions and the availability of multiple accessible redox states[19]. The insertion of Li-ions in V_2O_5 brings about a series of phase transformations, which can result in considerable heterogeneity of lithiation across electrode architectures[20,21]. As such, the effective utilization of this

material requires an understanding of how to structure the material in the form of a porous electrode such that the deleterious impact of phase heterogeneities can be alleviated[9,22].

In this study, we map the phase progression and mesoscale response of electrode architectures by comparing electrodes comprising α-V_2O_5 nanospheres (NS V_2O_5) with diameters of 49 ± 7 nm with electrodes constructed from micrometre-sized platelets of α-V_2O_5 (denoted as bulk V_2O_5, irregularly shaped platelets). Operando synchrotron X-ray diffraction is used to detect phase progression across the cathode geometry as a function of lithiation and delithiation. Operando synchrotron energy dispersive X-ray diffraction (EDXRD) is used to map layer-wise spatiotemporal evolution of phase heterogeneities across electrodes[23,24]. Electrodes comprising micrometre-sized particles exhibit a greater loss of accessible capacity as well as greater accumulation of stress compared with their nanometre-sized counterparts. Both phenomena are directly attributable to pronounced modification of the (transient) lithiation phase diagram of V_2O_5 and the much greater phase heterogeneity developed in micrometre-sized V_2O_5 particles as a result of geometry-dependent nucleation and transport limitations, as corroborated by phase-field modelling[25].

These measurements have been combined with focused ion beam–scanning electron microscope (FIB-SEM) tomography, electrochemical impedance spectroscopy (EIS) and mesoscale modelling of three-dimensional (3D) electrodes. The combined

[1]Department of Chemistry, Texas A&M University, College Station, TX, USA. [2]Department of Materials Science and Engineering, Texas A&M University, College Station, TX, USA. [3]Institute of Materials Science, Mechanics of Functional Materials, Technische Universität Darmstadt, Darmstadt, Germany. [4]Chemical Sciences & Engineering Division, Argonne National Laboratory, Lemont, IL, USA. [5]Department of Mechanical Engineering, Texas A&M University, College Station, TX, USA. [6]School of Mechanical Engineering, Purdue University, West Lafayette, IN, USA. [7]X-ray Science Division, Argonne National Laboratory, Lemont, IL, USA. ✉e-mail: pmukherjee@purdue.edu; xu@mfm.tu-darmstadt.de; banerjee@chem.tamu.edu

experimental and modelling studies hereby demonstrate: (1) geometry-dependent modification of the lithiation-induced phase transformations of V_2O_5, enabling expanded metastable regimes in the lithiation phase diagram; and (2) particle geometry-dependent variation of electrode tortuosity, engendering ion-transport limitations in thicker electrodes.

Electrochemistry–mechanics coupling

Micrometre-sized 'bulk V_2O_5' particles have a platelet-like morphology with lateral dimensions ranging from 300 nm to 10 μm, and thicknesses spanning several hundred nanometres (Fig. 1a). NS V_2O_5 were synthesized as described in the Methods. The V_2O_5 nanospheres are approximately 49 ± 7 nm in diameter (Fig. 1d). The nanospheres, as well as bulk V_2O_5, are crystallized as the orthorhombic polymorph of V_2O_5 (Fig. 1a,d,g).

Figure 1b,e contrasts galvanostatic measurements acquired for bulk and NS V_2O_5 in the voltage window between 2.8 and 4.0 V, corresponding to reversible lithiation-induced phase transformations to α-$Li_xV_2O_5$ ($x \approx 0$–0.1), ε-$Li_xV_2O_5$ ($x \approx 0.3$–0.7) and then to δ-$Li_xV_2O_5$ ($x \approx 0.8$–1.0). Both bulk and NS V_2O_5 exhibit two plateaus at 3.38 and 3.19 V, consistent with reduction features at 3.34 and 3.14 V, as shown in Fig. 1c,f, respectively, which are specifically attributable to α-$V_2O_5 \rightarrow$ε-$Li_xV_2O_5$ and ε-$Li_xV_2O_5 \rightarrow$δ-$Li_xV_2O_5$ transformations[26–28]. Bulk V_2O_5 exhibits considerably greater hysteresis between charge and discharge plateaus compared with NS V_2O_5. An additional oxidation peak at 3.34 V in the cyclic voltammetry (CV) curve and a brief plateau at 3.27 V in the charge profile are observed for bulk V_2O_5, but not for NS V_2O_5, and are ascribed to notable differences in phase transformation behaviour (below). When cycled at a C rate of C/2, NS V_2O_5 achieves a relatively high discharge capacity of 152.8 mAh g^{-1} in the second cycle and retains a capacity of 128.5 mAh g^{-1} after 100 cycles; in contrast, bulk V_2O_5 has a capacity of 112.3 mAh g^{-1} after the second cycle, which decreases to 101.3 mAh g^{-1} after 100 cycles (Fig. 1h).

Multibeam optical sensor (MOS) measurements in Fig. 1i show that the magnitude of stress variation for bulk V_2O_5 increases from 5.0 to 19.2 MPa between the discharged and charged states after 40 cycles, whereas this differential (1.5 to 4.4 MPa) is much smaller for NS V_2O_5 (Supplementary Fig. 2). Laboratory X-ray diffraction patterns (Supplementary Fig. 3 and Rietveld refinement statistics in Supplementary Table 1) illustrate that the greater stresses observed for the larger particles derive from irreversible lithiation and greater phase heterogeneity.

Structural origins of particle geometry-variant effects

To illuminate the structural origins of the particle geometry-dependent differences, operando high-resolution synchrotron diffraction measurements have been performed, as shown in Fig. 2. The lattice parameters extracted from Rietveld refinements are plotted in Fig. 3a,b alongside the structures of the lithiated phases and the inferred phase coexistence regimes for bulk and NS V_2O_5 (Rietveld refinement statistics in Supplementary Tables 2–5). While such measurements are subject to low statistics, operando X-ray diffraction data acquired for multiple cycles for bulk and NS V_2O_5 are shown in Supplementary Fig. 4 and are consistent with the observations of Fig. 2. It is worth noting that these represent ensemble (and not particle-by-particle) measurements.

For bulk V_2O_5 electrodes, during discharge, subtle shifts of (001) and (101) reflections at a nominal concentration of $Li_{0.08}V_2O_5$ mark the emergence of the slightly lithiated α-$Li_xV_2O_5$ phase (Fig. 2d), which retains the orthorhombic unit cell of V_2O_5. At 3.32 V, at a nominal concentration of $Li_{0.30}V_2O_5$, reflections characteristic of ε-$Li_xV_2O_5$ appear (Fig. 2d). Figure 3c displays the ε-$Li_xV_2O_5$ structure characterized by an increase of the interlayer spacing and canting of the apical vanadyl moieties. A substantial coexistence regime between α-$Li_xV_2O_5$ and ε-$Li_xV_2O_5$ is identified

spanning $x \approx 0.08$–0.30 (Fig. 3a). The ε-$Li_xV_2O_5$ phase grows in intensity with increasing lithiation (Fig. 2b,d) and monotonic shifts are observed corresponding to an extended solid-solution lithiation regime between $Li_{0.30}V_2O_5$ and $Li_{0.80}V_2O_5$. The splitting of the 3.0 Å reflection at $Li_{0.88}V_2O_5$ denotes the emergence of a highly lithiated ε′-$Li_xV_2O_5$ phase (Fig. 3c), which is characterized by a considerable rearrangement of Li-ion occupancies, but with retention of the puckered single-layered ε-$Li_xV_2O_5$ framework[29,30]. On still further Li-ion intercalation, to $Li_{0.92}V_2O_5$ at 2.80 V, new reflections emerge that are characteristic of the δ-$Li_xV_2O_5$ phase; Fig. 3c shows the structure of the δ phase characterized by a shifting of alternate layers by half a unit cell along the b axis. As such, a phase coexistence regime encompassing ε-, ε′- and δ-$Li_xV_2O_5$ is observed within the potential window from 3.16 to 2.80 V (Supplementary Fig. 5a and Rietveld refinement statistics in Supplementary Table 6).

During the charging process, Fig. 2b shows a reverse sequence of transformations from δ-$Li_xV_2O_5 \rightarrow$ε-$Li_xV_2O_5$ as well as ε′-$Li_xV_2O_5 \rightarrow$ε-$Li_xV_2O_5$. However, δ-$Li_xV_2O_5$ persists down to $Li_{0.47}V_2O_5$ at a voltage of 3.38 V, denoting the considerable overpotential needed to delithiate micrometre-sized particles, as also observed in Fig. 1b. A substantial concentration of ε-$Li_xV_2O_5$ is observed at the end of the charging process (Supplementary Fig. 6b and Rietveld refinement statistics in Supplementary Table 7). With more cycles, the phase coexistence of ε-, ε′- and δ-$Li_xV_2O_5$ at the end of the discharged state is observed and the concentration of ε-$Li_xV_2O_5$ at the end of charged state increases (Fig. 2f, Supplementary Figs. 5 and 6, which explain the loss of reversible capacity in Fig. 1b, and Supplementary Fig. 7a).

The phase evolution of NS V_2O_5 on electrochemical cycling shows notable differences, as shown in Figs. 2c,e and 3b. Initial lithiation to $Li_{0.10}V_2O_5$ brings about phase transformation of V_2O_5 to α-$Li_xV_2O_5$. With further lithiation to $Li_xV_2O_5$ ($x = 0.10$–0.35), phase coexistence of α-$Li_xV_2O_5$ and ε-$Li_xV_2O_5$ is again observed, as shown in Fig. 3b. The origins of this phase coexistence are discussed below in light of the characterization of particle connectivity by FIB-SEM tomography and EIS measurements. With greater lithiation, the ε′-$Li_xV_2O_5$ phase is stabilized. Indeed, solid-solution formation within ε/ε′-$Li_xV_2O_5$ is observed across an extended potential window but without emergence of the δ-$Li_xV_2O_5$ phase. Specifically, phase coexistence of ε-$Li_xV_2O_5$/δ-$Li_xV_2O_5$ observed in bulk V_2O_5 is supplanted in NS V_2O_5 by single-phase solid-solution formation across ε/ε′-$Li_xV_2O_5$ (Fig. 3b)[31–33]. The extended metastability of the single-phase regime results from the relatively greater penalties to forming phase boundaries, more uniform local chemical potentials and the reduced bulk transport limitations within nanometre-sized particles. As such, the incoming Li-ion flux is accommodated through stabilization of ε′-$Li_xV_2O_5$ (which simply requires a change of cation ordering) instead of nucleation of δ-$Li_xV_2O_5$ (which requires a substantial structural rearrangement). As sketched in Fig. 3a,b, particle geometry effects strongly modify the progression of intercalation-induced transformations in $Li_xV_2O_5$. Further, the decreased phase heterogeneity observed for NS V_2O_5 is the origin of the substantially lower stress accumulated in such electrodes (Fig. 1i), since ε and ε′ polymorphs form much more commensurate interfaces compared with ε/δ phase boundaries.

The NS V_2O_5 electrode further shows notable differences on cycling. Li-ions are sequentially extracted from ε′-$Li_xV_2O_5 \rightarrow$ε-$Li_xV_2O_5 \rightarrow$α-$Li_xV_2O_5 \rightarrow V_2O_5$ with narrow coexistence windows and recovery of unlithiated V_2O_5 (Supplementary Figs. 8b, 9 and 10 and Rietveld refinement statistics in Supplementary Tables 8 and 9). As such, NS V_2O_5 electrodes show a higher accessible capacity on prolonged electrochemical cycling (Fig. 1e and Supplementary Fig. 7b) with much reduced stress accumulation directly traceable to the decreased heterogeneity (Fig. 1i). On the basis of the operando measurements, reversible reduction peaks at 3.34 and 3.14 V (Fig. 1f) correspond to phase transformations of α-$V_2O_5 \rightarrow$ε-$Li_xV_2O_5$
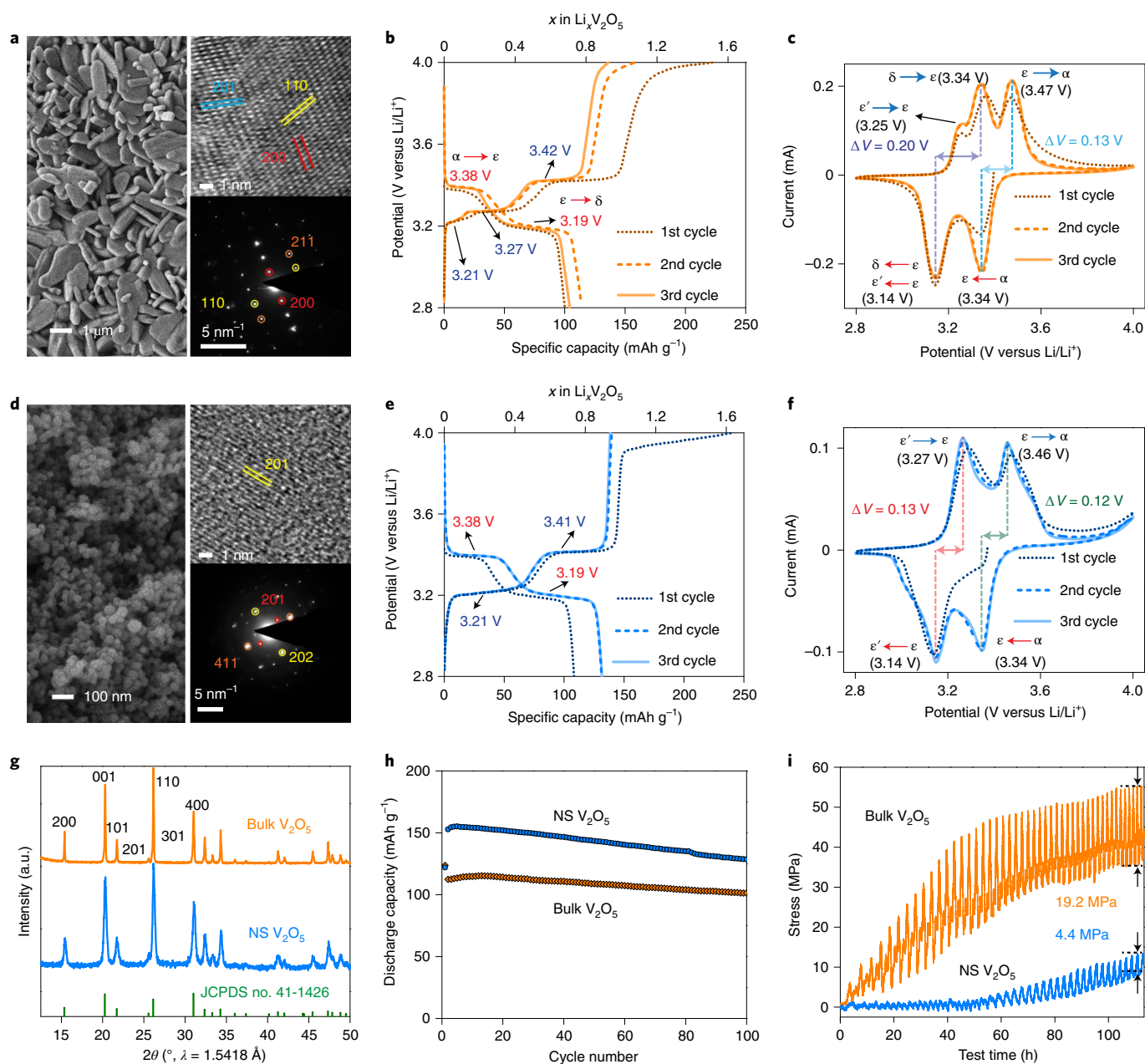
Fig. 1 | Morphology and electrochemical characterization of bulk and NS V₂O₅. a, SEM images (left), lattice-resolved TEM images (top right) and selected area electron diffraction patterns (bottom right) of bulk V_2O_5). **b**, Galvanostatic discharge and charge profiles at C/20 measured for bulk V_2O_5). **c,f**, Initial three cycles of cyclic voltammetry sweeps in the 2.8–4.0 V potential range of bulk V_2O_5 (**c**) and NS V_2O_5 (**f**). Comparing the relative polarization, values of 0.12 and 0.13 V are observed for NS V_2O_5, respectively, compared with 0.13 and 0.20 V for bulk V_2O_5 (**c** and **f**). **d**, SEM images (left), lattice-resolved TEM images (top right) and selected area electron diffraction patterns (bottom right) of NS V_2O_5. **e**, Galvanostatic discharge and charge profiles at C/20 measured for NS V_2O_5. **g**, Laboratory powder X-ray diffraction patterns of bulk and NS α-V_2O_5. **h**, Discharge capacity of bulk V_2O_5 and NS V_2O_5 at C/2 between 2.8 and 4.0 V for 100 cycles. **i**, Electrochemistry-coupled MOS stress measurements during cycling between 2.8 and 4.0 V at C/5 for 40 cycles measured for bulk V_2O_5 and NS V_2O_5. The potential range of 2.8–4.0 V was selected for galvanostatic measurements to avoid irreversible phase transformations to γ- and ω-$Li_xV_2O_5$ phases at deeper depths of discharge. Supplementary Fig. 1 plots CV and galvanostatic discharge/charge profiles in an expanded potential range of 2.0—4.0 V for bulk and NS V_2O_5, which show irreversible phase transformations from δ-$Li_xV_2O_5$→γ-$Li_xV_2O_5$ and γ-$Li_xV_2O_5$→ω-$Li_xV_2O_5$.

(formally, a first-order phase transition), and from ε-$Li_xV_2O_5$→ε′-$Li_xV_2O_5$ (a Li-ion ordering transition) within NS V_2O_5 (ref. [30]). In contrast, for bulk V_2O_5 (Fig. 1c), the α-V_2O_5→ε-$Li_xV_2O_5$ transition is observed at 3.34 V and concurrent reductions are observed from ε-$Li_xV_2O_5$ to ε′-$Li_xV_2O_5$ and δ-$Li_xV_2O_5$ at 3.14 V. The oxidation peaks at 3.25 and 3.34 V observed for bulk V_2O_5 are ascribed to ε′-$Li_xV_2O_5$→ε-$Li_xV_2O_5$ and δ-$Li_xV_2O_5$→ε-$Li_xV_2O_5$

transformations, respectively. The latter is not observed in NS V_2O_5 and is a result of the sluggish kinetics and extended phase coexistence regimes within bulk V_2O_5.

To understand particle geometry effects, a phase-field model for mechanically coupled Cahn–Hilliard-type diffusion has been implemented to simulate the spatiotemporal distribution of Li-ions (Fig. 3d,e). The random packing algorithm from GeoDict has been
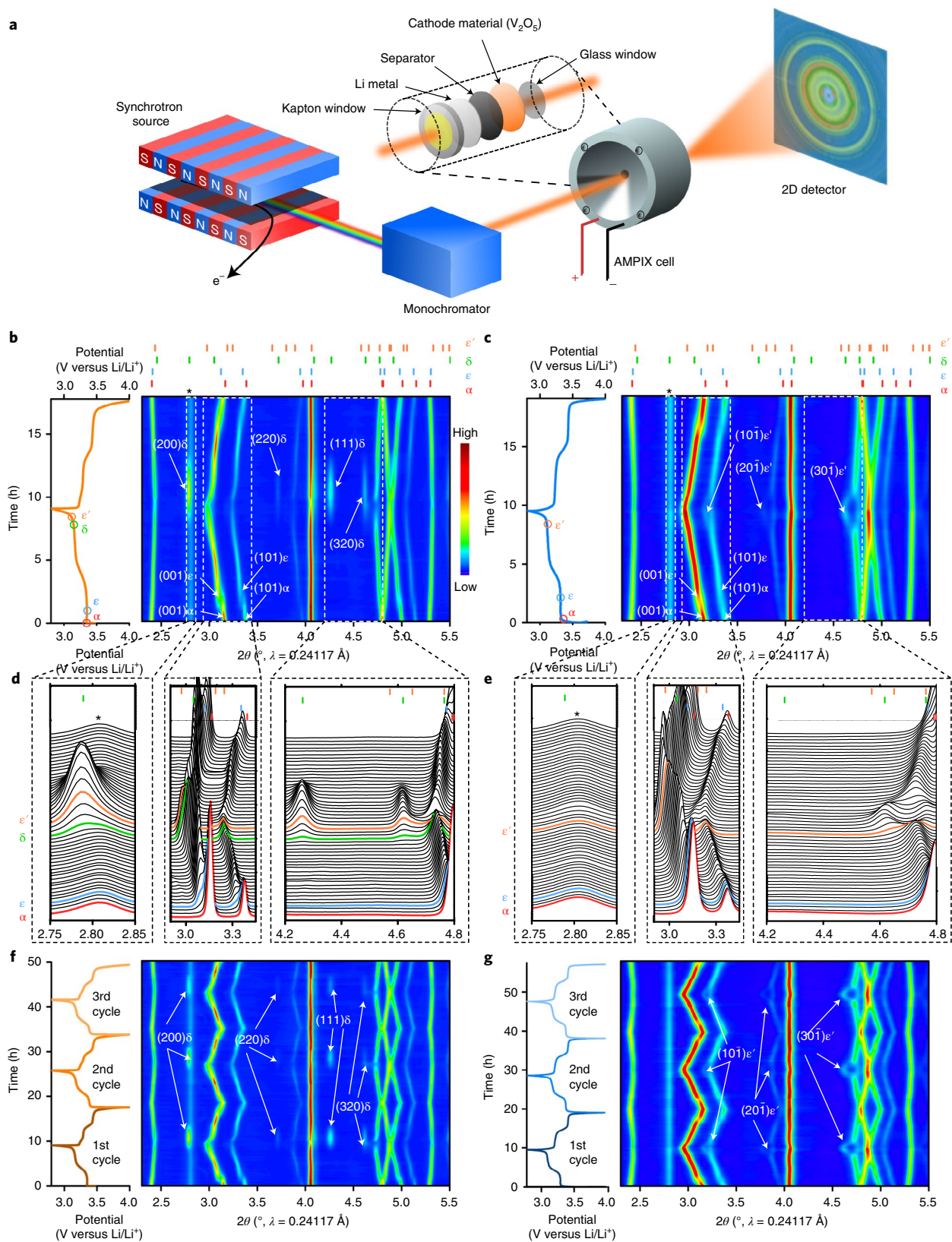
Fig. 2 | Operando synchrotron XRD measurements. a, Schematic depiction of operando synchrotron X-ray diffraction set-up. **b,c**, Contour plots (right panels) of operando synchrotron X-ray diffraction and corresponding galvanostatic discharge/charge profiles (left panels) of bulk V_2O_5 (**b**) and NS V_2O_5 (**c**) in the first cycle. For bulk V_2O_5, the electrode comprises 24.5% ε-$Li_xV_2O_5$, 57.3% ε'-$Li_xV_2O_5$ and 18.2% δ-$Li_xV_2O_5$ at the end of the discharge state of the first cycle (Supplementary Fig. 5a). Red ticks: α-V_2O_5; blue ticks: ε-$Li_xV_2O_5$; orange ticks: ε'-$Li_xV_2O_5$; green ticks: δ-$Li_xV_2O_5$. Asterisks denote reflections from carbon materials used in the electrode assembly. **d,e**, Magnified views of representative X-ray diffraction patterns in selected regions (marked as dashed line boxes in **b** and **c**) of bulk V_2O_5 (**d**) and NS V_2O_5 (**e**). **f,g**, Contour plots (right panels) showing operando synchrotron X-ray diffraction data in the first three cycles and corresponding galvanostatic discharge/charge profiles (left panels) measured for bulk V_2O_5 (**f**) and NS V_2O_5 (**g**).
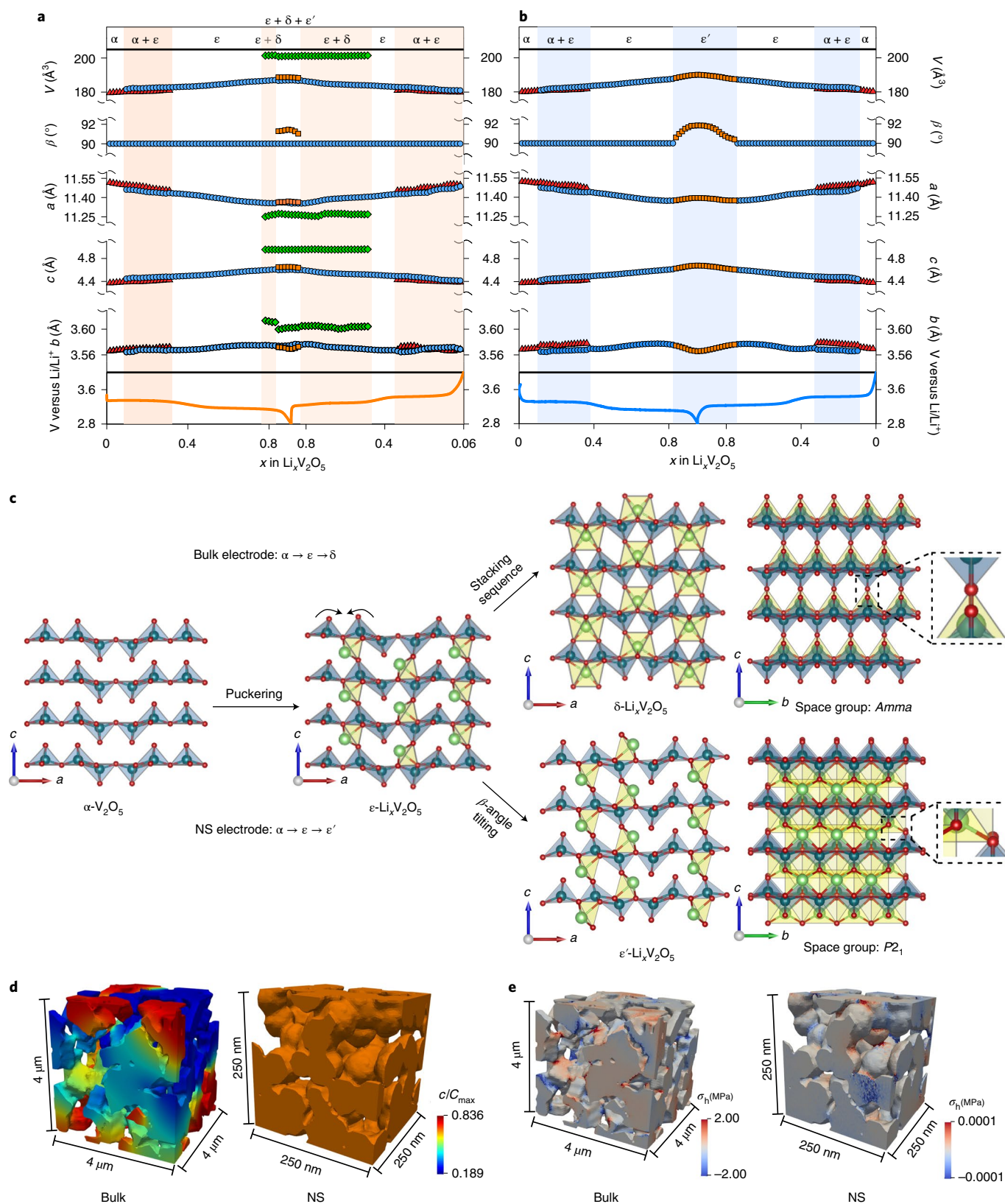
Fig. 3 | Particle geometry dependence of (transient) lithiation phase diagram. Profoundly different lithiation phase diagrams are observed for bulk platelets and NS V_2O_5. **a,b**, Evolution of lattice parameters obtained from Rietveld refinement to X-ray diffraction patterns (in Fig. 2b,c) as a function of potential/x in $Li_xV_2O_5$ (bottom) for bulk V_2O_5 (**a**) and NS V_2O_5 (**b**). V is the unit cell volume and β is the angle between the a and c vectors. **c**, Crystal structures of α-V_2O_5, ε-$Li_xV_2O_5$, ε'-$Li_xV_2O_5$ and δ-$Li_xV_2O_5$. Red, blue and green spheres represent oxygen, vanadium and lithium atoms, respectively; the blue and yellow pyramids represent $[VO_x]$ and $[LiO_y]$ units. **d**, Lithium concentration distribution obtained from phase-field simulations of bulk V_2O_5 (left) and NS V_2O_5 (right) electrodes. **e**, Normalized hydrostatic stress distribution inside the electrode acquired from phase-field simulations for bulk V_2O_5 (left) and NS V_2O_5 (right). In the bulk V_2O_5, tensile stress is prominent at the necking of the platelets. Details of modelling are provided in the Methods.

used to create the NS and bulk V_2O_5 microstructures (Methods). The cube size of the bulk V_2O_5 cathode is $4\,\mu m \times 4\,\mu m \times 4\,\mu m$, which is randomly filled by a small orthogonal brick with dimensions of $1.2\,\mu m \times 0.7\,\mu m \times 0.3\,\mu m$. The cube size of the NS V_2O_5 cathode is $250\,nm \times 250\,nm \times 250\,nm$, and is filled with spherical particles with a diameter of $60\,nm$. These geometries are derived from scanning electron microscopy (SEM)/transmission electron microscopy (TEM) images, as shown in Fig. 1a,d and as further verified by tomography measurements discussed below.

Concordant with operando synchrotron X-ray diffraction results, for the same discharge state, Fig. 3d shows that a porous electrode constructed from larger platelets shows considerable phase heterogeneity, whereas minimal heterogeneity is observed for a porous electrode constructed from V_2O_5 nanospheres (Supplementary Fig. 11, showing plots of concentration distribution). The specific patterns of heterogeneities observed for the larger platelets are determined by geometric and dimensional effects and are reflective of the interplay between surface reaction-limited nucleation processes and bulk transport limitations[7,22,34]. Both the nucleation barrier and transport limitations are diminished for the nanospheres, which furthermore circumvent phase separation through extended lithiation across the ε/ε'-$Li_xV_2O_5$ solid solution. Figure 3e contrasts the normalized hydrostatic stress distributions of bulk V_2O_5 and NS V_2O_5 particles. Consistent with MOS measurements, bulk V_2O_5 engenders a much greater magnitude of the stress compared with NS V_2O_5.

These results indicate a pronounced alteration of phase progression as a function of particle geometry. The consequences of non-uniform local chemical potentials and transport limitations are considerably greater phase heterogeneities in bulk V_2O_5 platelets, which, over multiple discharge/charge cycles, diminish the accessible capacity and result in the generation of substantial stress gradients. In contrast, extended solid-solution regimes are observed for NS V_2O_5, which shows sequential transformations with narrow phase coexistence regimes, complete delithiation, retention of capacity and minimal stress accumulation.

Mapping spatiotemporal evolution of lithiated phases

Operando EDXRD provides a means of interrogating mesoscale phase inhomogeneities and mapping the spatiotemporal evolution of phase fronts across the thickness of the electrode (Supplementary Videos 1 and 2). As sketched in Fig. 4a, we have acquired data across three middle segments of the active electrode. The (001) lattice plane of V_2O_5 is used as a diagnostic of lithiation gradients and phase evolution within the three segmented regions of bulk and NS V_2O_5 electrodes, as shown in Fig. 4b,d. Intensity modulation across the different layers corresponds to spatial gradients in the extent of lithiation (and phase evolution) across the electrodes, whereas broadened reflections denote phase coexistence within each layer. Figure 4b,d clearly contrasts the varying extents of phase heterogeneity in bulk and NS V_2O_5 electrodes. The corresponding diffraction patterns are plotted in Supplementary Figs. 12 and 13. We note consistent electrochemical performance across Fig. 1b,e and Supplementary Fig. 7 corresponding to electrochemical data acquired during operando synchrotron X-ray diffraction measurements, and in Supplementary Fig. 14 corresponding to EDXRD measurements.

During initial lithiation of the bulk V_2O_5 electrode, Fig. 4b illustrates the uniform formation of α-$Li_xV_2O_5$ across the layers. With increasing lithiation as ε-$Li_xV_2O_5$ is nucleated, as shown in Fig. 4b, phase coexistence of α- and ε-$Li_xV_2O_5$ is observed up to a voltage of 3.20 V. The relative ratio of ε- to α-$Li_xV_2O_5$ increases from layer 3 to layer 5, showing a gradient in phase evolution correlated directly with the Li-ion flux. δ-$Li_xV_2O_5$ is initially observed at $x = 0.65$, 3.18 V, leading to the coexistence of ε- to δ-$Li_xV_2O_5$ with a gradient across layers. ε'-$Li_xV_2O_5$ appears at $x = 0.75$, 3.16 V. Phase

coexistence of ε-, δ- and ε'-$Li_xV_2O_5$ is observed until the end of the discharged state at 2.8 V spanning $x \approx 0.75$–0.87. Phase heterogeneity is observed within individual layers as well across the thickness of the electrode.

During the initial charging process, reflections at 4.65 Å disappear at $x = 0.79$, 3.27 V, indicating the complete delithiation and transformation of ε'-$Li_xV_2O_5$ (Fig. 4b). This is followed by the delithiation of both δ- and ε-$Li_xV_2O_5$. δ-$Li_xV_2O_5$ is entirely transformed beyond 3.43 V, whereas ε-$Li_xV_2O_5$ starts to transform into α-$Li_xV_2O_5$ at $x = 0.32$, 3.44 V. At this voltage, α-$Li_xV_2O_5$ is only present in layer 5, whereas layers 3 and 4 show ε-$Li_xV_2O_5$. Indeed, the interfacial layer in contact with the electrolyte has been delithiated, thereby stranding Li-ions within the interior of the electrode architecture that are subject to ion-transport limitations (below). As such, the cut-off voltage is reached prematurely before Li-ions are completely extracted from the cathode, which results in capacity fading on prolonged cycling. By the end of charging, mixtures of ε- and α-$Li_xV_2O_5$ are observed. It is worth noting that ε'-$Li_xV_2O_5$ is delithiated to ε-$Li_xV_2O_5$ before delithiation of δ-$Li_xV_2O_5$ despite its relatively lower Li content. In light of the coherent ε/ε'-$Li_xV_2O_5$ interface, delithiation can proceed with reordering of Li-ions between the layers, whereas delithiation of δ-$Li_xV_2O_5$ requires nucleation of the ε-$Li_xV_2O_5$ phase. Furthermore, for bulk V_2O_5, the delayed as well as asymmetric lithiation/delithiation (Supplementary Fig. 14a) are a result of spatiotemporal phase inhomogeneities across the thickness of the bulk V_2O_5 electrode.

For NS V_2O_5, no phase coexistence is observed within individual layers, indicating homogeneous phase transformations from α-$V_2O_5 \rightarrow \alpha$-$Li_xV_2O_5 \rightarrow \varepsilon$-$Li_xV_2O_5 \rightarrow \varepsilon'$-$Li_xV_2O_5$. Between segmented layers, lithiation-induced phase transformations from α- to ε-$Li_xV_2O_5$ and ε- to ε'-$Li_xV_2O_5$ result in modest gradients from layer 3 to 5 at potential plateaus at 3.38 and 3.19 V, respectively (Supplementary Fig. 14b). The interlayer separation does increase across layers 3–5, indicative of increased lithiation at the layer closer to the electrolyte interface, albeit phase propagation is sufficiently rapid as to ensure phase homogeneity across the thickness of the electrode. In contrast to bulk V_2O_5 and consistent with the operando X-ray diffraction results, no formation of δ-$Li_xV_2O_5$ is observed down to 2.8 V. The delithiation of NS V_2O_5 entirely mirrors the lithiation process, with no discernible inhomogeneity within individual layers and only modest gradients across layers. α-V_2O_5 is obtained without detectable lithiated phases at the end of delithiation. As such, these observations are consistent with well-defined phase transformations at potential plateaus and the stabilization of phase-pure $Li_xV_2O_5$ at slopes for electrodes comprising V_2O_5 nanospheres, which provides a notable contrast to the extended phase coexistence regimes and spatiotemporal heterogeneity observed for bulk V_2O_5 electrodes.

For electrodes constituted from micrometre-sized platelets of V_2O_5, considerable phase heterogeneities are observed within individual segmented layers and across the thickness of the electrodes. The phase heterogeneity is exacerbated with continuous cycling (Fig. 5). The rapid delithiation of layers closest to the electrolyte and the ensuing structural transformations that hinder Li-ion diffusion[22,26], leave stranded lithiated domains within the interior of the electrode, thereby representing a primary origin of capacity fade. In contrast, phase homogeneity across the entire electrode thickness, as well as symmetric and complete lithiation/delithiation, is observed for electrodes comprising NS V_2O_5.

To understand differences between bulk and NS V_2O_5, the potential variation and diffusion of Li-ions have been modelled, as shown in Fig. 6 and detailed in the Methods (see 'evolution of electrolyte concentration' in Supplementary Fig. 15). Stoichiometric gradients can manifest at multiple length scales in response to different forms of transport limitations. To assess the relevance of particle-scale transport limitations, the deduced timescales for particle-scale diffusion (Methods) are $t_s^{spherical} \approx 0.5\,s$ and $t_s^{platelet} \approx 50\,s$, which are
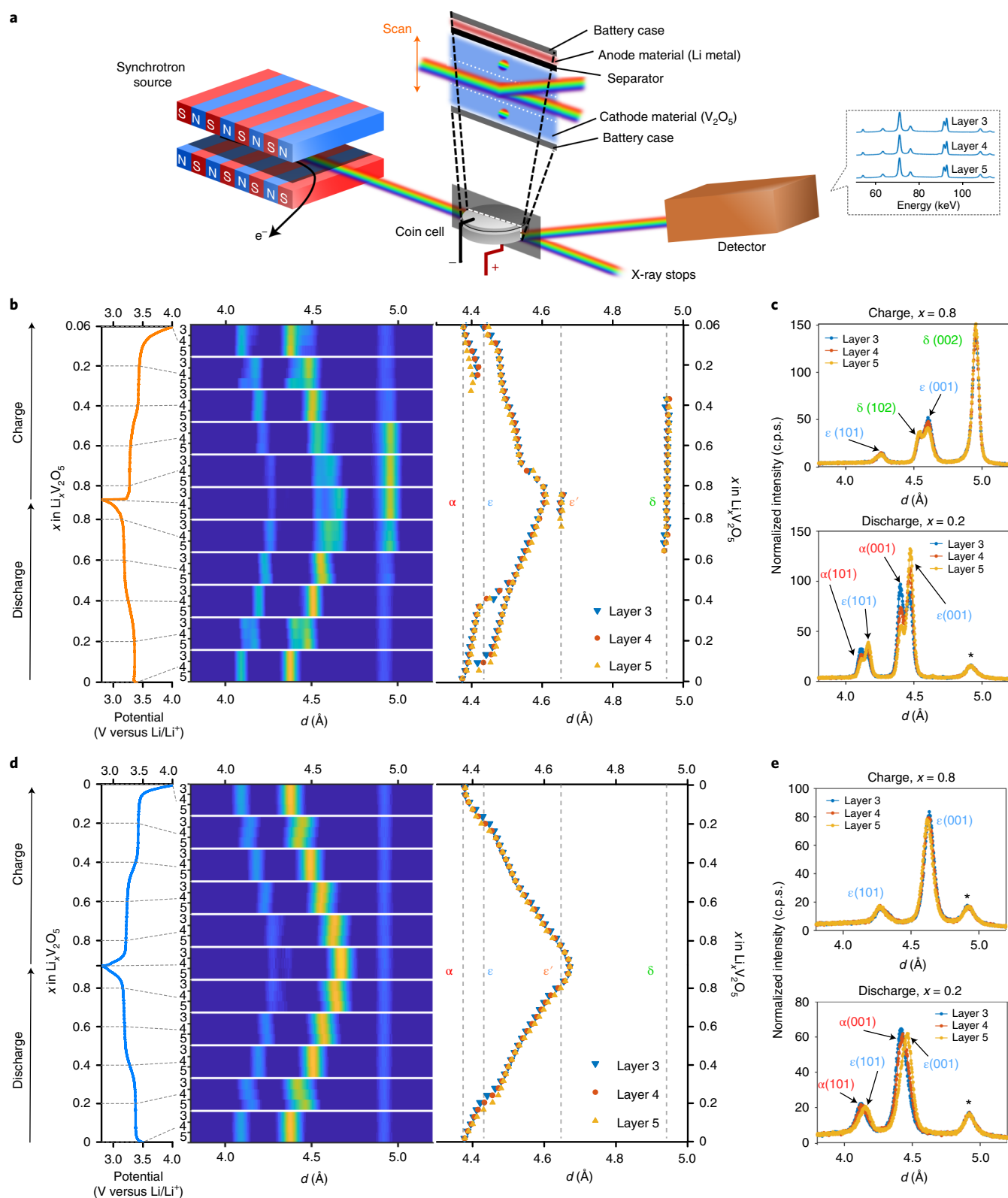
Fig. 4 | Mapping spatiotemporal phase evolution across the thickness of an electrode. a, Schematic depiction of operando synchrotron EDXRD set-up. EDXRD data were acquired for seven layers (each spanning 30 μm in thickness) at the centred area of the coin cell. Data for layers 3 (blue), 4 (red) and 5 (yellow) are shown, illustrating phase evolution as a function of the distance between the electrode and the separator. With reference to the separator, layer 3 is the furthest away, layer 4 is in the middle and layer 5 is the closest to the separator. Li-ion intercalation is initiated from layer 5 and propagates through to layer 3. **b,d,** Corresponding galvanostatic discharge/charge profile (left), selected contour maps between 3.8 and 5.2 Å from layer 3 to layer 5 (middle) and selected representative diffraction patterns (right) as a function of potential/$Li_xV_2O_5$ for bulk V_2O_5 (**b**) and NS V_2O_5 (**d**). Diffraction patterns corresponding to the complete set of contour plots in **b** and **d** are presented in Supplementary Figs. 12 and 13, respectively. Asterisks denote reflections from carbon materials used in the electrode assembly. **c,e,** Selected diffraction patterns for bulk V_2O_5 (**c**) and NS V_2O_5 (**e**). c.p.s., counts per second.
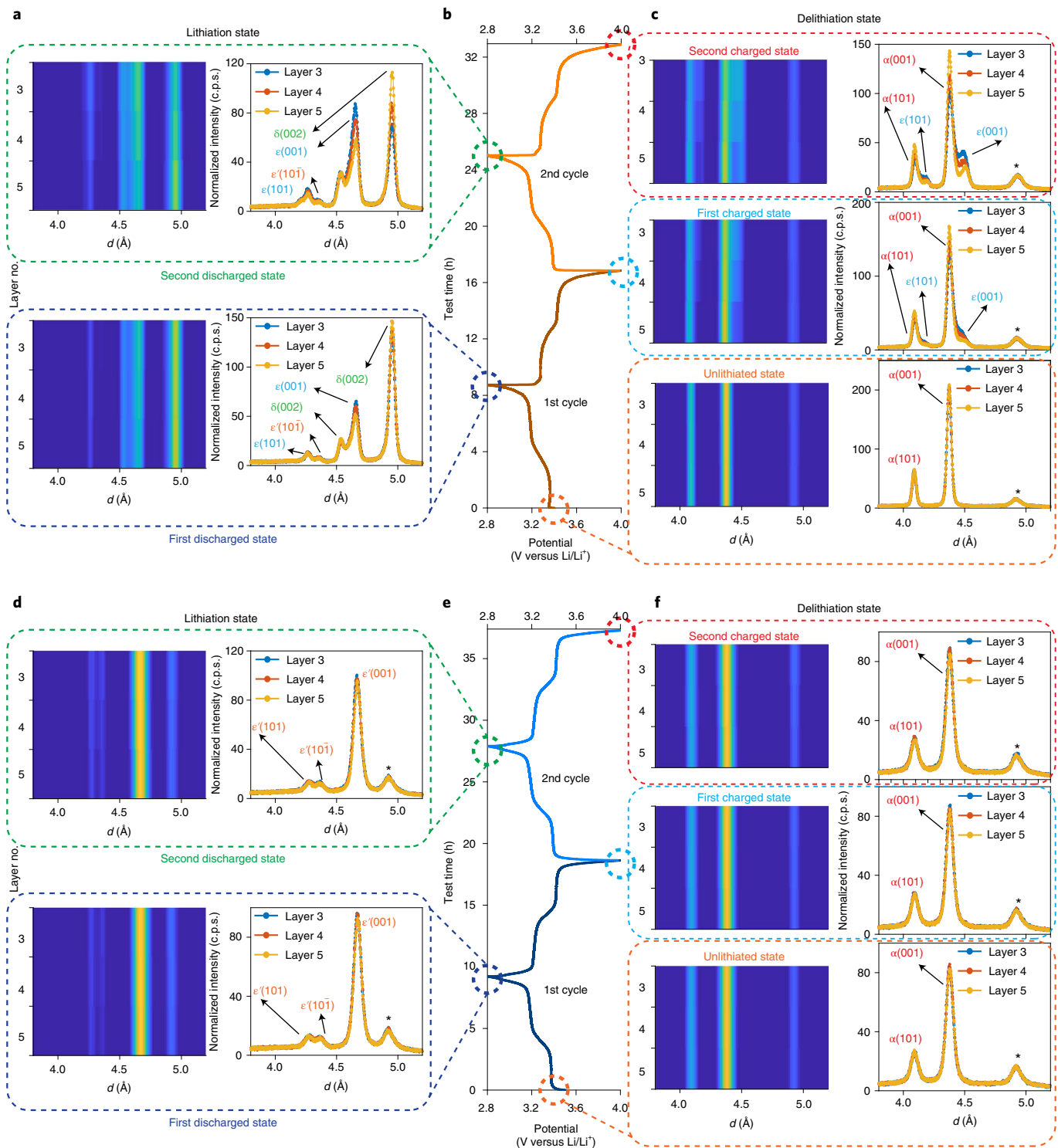
Fig. 5 | Mapping accumulation of phase heterogeneities using operando synchrotron EDXRD measurements of bulk and NS V₂O₅ electrodes.
a,d, Contour plots and correlated diffraction patterns between 3.8 and 5.2 Å from layers 3 to 5 on lithiation (discharged to 2.8 V) for bulk (**a**) and NS V₂O₅ (**d**). **b,e**, Galvanostatic discharge/charge profiles for two cycles at C/20 for bulk (**b**) and NS V₂O₅ (**e**). **c,f**, Contour plots and corresponding diffraction patterns between 3.8 and 5.2 Å from layers 3 to 5 on delithiation (charged to 4.0 V) for bulk (**c**) and NS V₂O₅ (**f**). For bulk V₂O₅ at delithiation state, the proportion of ε- to α-Li$_x$V₂O₅ decreases from layer 3 to 5, consistent with Li-ions being trapped within interiors of the electrode architecture. Asterisks denote reflections from carbon materials used in the electrode assembly. Operando EDXRD measurements have further been performed for a second cycle to characterize the spatial distribution of accumulated lithiated domains for both bulk and NS V₂O₅ as shown in the top panels in **a,c** and **d,f**. Extensive coexistence of ε-, ε′- and δ-Li$_x$V₂O₅ is detected for bulk V₂O₅. Phase heterogeneity is exacerbated with more extensive cycling. In contrast, EDXRD data for NS V₂O₅ show the notable absence of δ-Li$_x$V₂O₅, as well as homogeneous lithiation across layers 3 to 5 during both the first and the second discharge cycles. Comparing delithiation, EDXRD patterns suggest that all of the intercalated Li-ions are extracted from the electrode, which is consistent with the retention of capacity shown in Supplementary Fig. 14b.
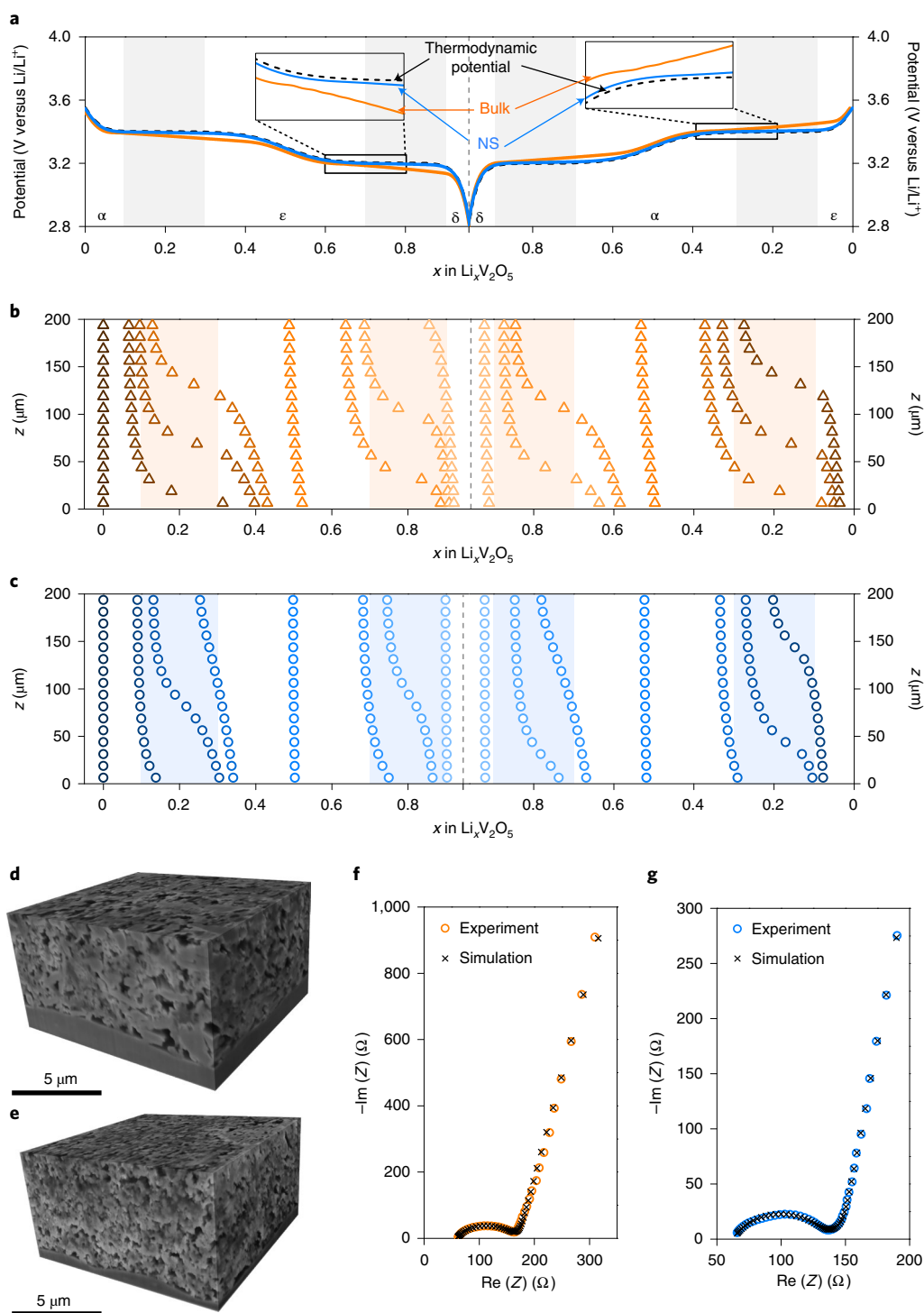
Fig. 6 | Mesoscale simulations of potential variation and Li-ion diffusion across the thickness of a composite electrode. a, Potential variation of the V_2O_5 electrodes contrasting bulk and NS morphologies as a function of lithiation/delithiation states. **b,c**, Distribution of intercalated/deintercalated lithium along the electrode thickness over time with bulk V_2O_5 (**b**) and with NS V_2O_5 (**c**). Single-phase regions with α, ε and δ are not shaded, whereas the two-phase $\alpha+\varepsilon$ and $\varepsilon+\delta$ regions are shaded. Li-ion intercalation (left panels of **a**–**c**) and deintercalation (right panels of **a**–**c**) across porous V_2O_5 electrodes. **d,e**, FIB-SEM three-dimensional tomography with $10\times10\times10\,\mu m^3$ dimensions for bulk V_2O_5 (**d**) and NS V_2O_5 (**e**) (the bottom layer is the aluminium foil current collector). **f,g**, Simulated Nyquist plots of the internal impedance for a symmetric cell by the S-GTLM under blocking condition of bulk V_2O_5 (**f**) and NS V_2O_5 (**g**). Differences in tortuosity strongly affect conductivity and ionic diffusivity, explaining differences observed in the function of porous electrode materials constructed from different particle dimensions and morphologies. The differences in tortuosity are seen to be a direct result of particle morphology differences.

substantially faster than the timescales of the current experiments (10 h at C/20). As such, diffusion limitations alone are unlikely to account for the observed mesoscale inhomogeneities[35]. Another

relevant limitation is ion transport within the electrolyte. For the electrodes examined in this work, ion-transport limitations can give rise to differences in intercalation at different distances from the

electrode/electrolyte interface on the basis of the local availability of Li-ions in the electrolyte. For such thick electrodes, one would generally expect preferential intercalation close to the separator where ions more easily arrive from the other electrode, whereas the interiors of the electrode architecture show a notable lag[36–38]. The morphology differences considered between the active particles considered here further compound this effect as platelets form more convoluted electrolyte transport pathways[39–42]. To obtain a 3D perspective of the electrode architecture, FIB-SEM tomography of bulk and NS V_2O_5 electrodes has been performed, as shown in Fig. 6d,e. The irregular shape and larger size of bulk V_2O_5 particles are clearly observed in Fig. 6d. Also, the connectivity between particles, binder and carbon materials is not evenly established, leading to the formation of pores with different sizes within the electrode. As such, an increased tortuosity can be inferred from Supplementary Video 3 relative to NS V_2O_5 (Fig. 6e and Supplementary Video 4). Accounting for such effects, the diffusion timescale in the electrolyte pore network is $t_e^{spherical} \approx 10$ min for NS V_2O_5, whereas $t_e^{platelet} \approx 1.2$ h for the bulk V_2O_5 electrode. Ion transport in the latter configuration is sluggish enough relative to the intercalation time of ~10 h to engender ionic gradients along the thickness of the electrodes (Fig. 6b). Under these operating conditions, intercalation is thus governed by local electrolyte gradients. As such, the electrode architecture built from active material, binder and carbon material plays a crucial role in affecting the Li-ion diffusion. For the same binder and carbon content with the same ratio of bulk and NS V_2O_5, the model captures the phase inhomogeneity observed in EDXRD. When the electrolyte concentration gradients are minimal, only small differences in the intercalation response of particles at different spatial locations are expected (Fig. 6c), as indeed observed in Figs. 4d and 5d–f for NS V_2O_5 electrodes. In contrast, when electrolyte transport is hindered, substantial intercalation gradients are expected along the electrode thickness (Fig. 6b), as observed for bulk V_2O_5 electrodes in Figs. 4b and 5a–c. Indeed, this further explains the greater total overpotential in two-phase regions seen in Fig. 6a. When the intercalation is halted at 2.8 V and deintercalation is initiated, the stoichiometric gradients are unable to relax, which thus compounds the stoichiometric polarization. Hence, the electrode with platelet particles exhibits a larger capacity difference, δQ, of 0.8% compared with 0.1% for the electrode with NS V_2O_5, explaining the capacity fading observed in bulk V_2O_5.

Tortuosity is a diffusional parameter that quantifies the complexity of ion transportation in a porous electrode. It is dominated by the microstructural pore-network complexity. To quantify electrode tortuosity, Nyquist impedance data of bulk and NS V_2O_5 in a blocking electrolyte have been fitted using a transmission line model[43] (Fig. 6f,g and Methods). For bulk and NS V_2O_5 electrodes, average tortuosity values of $\tau = 14.571$ and $\tau = 5.398$ are inferred, respectively. The tortuous pathways in bulk V_2O_5 electrodes result in restricted ionic transport and lower utilization of the active material. This is indicative of longer Li-ion diffusion pathways and lower active material–electrolyte contact areas. In contrast, NS V_2O_5 electrodes show lower tortuosity and maintain the homogeneity of ion distribution throughout the electrode, enabling improved macroscopic diffusivity and conductivity[41].

In summary, NS V_2O_5 exhibits a higher discharge capacity, substantially reduced polarization and is further characterized by a notably lesser extent of stress differentials between discharged and charged states. Operando synchrotron X-ray diffraction measurements demonstrate pronounced differences in lithiation phase diagrams as a function of particle geometry. Bulk V_2O_5 is characterized by extended phase coexistence regimes and transforms into highly lithiated δ-$Li_xV_2O_5$ on discharge. In contrast, NS V_2O_5 shows consecutive transformations with minimal phase coexistence. It has a strong proclivity to stabilize a highly lithiated ϵ'-$Li_xV_2O_5$ phase (characterized by reordering of Li-ion positions and a coherently

matched lattice) at the same depth of discharge instead of undergoing a distortive phase transformation to δ-$Li_xV_2O_5$. A distorted monoclinic crystal structure is identified for the ϵ'-$Li_xV_2O_5$ phase, which thus represents a distinct polymorph stabilized at nanometre-sized dimensions to circumvent the formation of lattice-mismatched phase boundaries. Lithiation and delithiation proceed symmetrically for NS V_2O_5, resulting in excellent reversibility. In contrast, the extended phase coexistence regimes observed for bulk V_2O_5 are the origin of the substantially greater polarization observed for electrodes constituted from larger particles. Phase-field modelling shows that particle geometry-dependent phase heterogeneities give rise to extensive stress accumulation for larger platelets compared with smaller nanospheres, which represents a primary origin of capacity fade.

Operando EDXRD results show much greater spatiotemporal heterogeneities within individual segmented layers and across the thickness of the electrode for electrode architectures constituted from larger platelets. The heterogeneities are compounded with further cycling as preferential delithiation at the electrode/electrolyte interface leaves stranded lithiated domains within the interior of the electrode architecture. Delithiation is observed to proceed preferentially from ϵ/ϵ'-$Li_xV_2O_5$ instead of the higher lithiated δ-$Li_xV_2O_5$. In contrast, NS V_2O_5 electrodes circumvent the formation of δ-$Li_xV_2O_5$ and show entirely homogeneous phase progression within individual layers and across the electrode thickness. Mesoscale modelling of spatial heterogeneities in conjunction with FIB-SEM tomography and electrochemical impedance modelling point to ion-transport limitations resulting from the higher tortuosity across the thickness of the electrode architectures for larger platelets as a major contributor.

As such, operando powder X-ray diffraction and EDXRD enable mapping of the structural origins of polarization, capacity fade and stress accumulation from atomic to mesoscale dimensions. The results demonstrate the pronounced particle geometry-dependent modification of transient phase diagrams, which has substantial implications for phase boundaries and resulting stress accumulation. Operando diffraction studies and associated phase-field and mesoscale modelling show that low porosity and high tortuosity in the bulk electrode are a direct result of particle geometry. These results offer key insights into the structural origins of critical aspects of electrochemical performance for phase-transforming electrodes and illuminate fundamental design principles for mitigating deleterious phase transformations and high tortuosity in the construction of electrode architectures.

Online content

Any methods, additional references, Nature Research reporting summaries, source data, extended data, supplementary information, acknowledgements, peer review information; details of author contributions and competing interests; and statements of data and code availability are available at https://doi.org/10.1038/s41563-021-01151-8.

References

1. Abakumov, A. M., Fedotov, S. S., Antipov, E. V. & Tarascon, J. M. Solid state chemistry for developing better metal-ion batteries. *Nat. Commun.* **11**, 4976 (2020).
2. Manthiram, A. A reflection on lithium-ion battery cathode chemistry. *Nat. Commun.* **11**, 1550 (2020).
3. Xie, J. & Lu, Y. C. A retrospective on lithium-ion batteries. *Nat. Commun.* **11**, 2499 (2020).
4. Goodenough, J. B. & Park, K. S. The li-ion rechargeable battery: a perspective. *J. Am. Chem. Soc.* **135**, 1167–1176 (2013).
5. Boebinger, M. G. et al. Spontaneous and reversible hollowing of alloy anode nanocrystals for stable battery cycling. *Nat. Nanotechnol.* **15**, 475–481 (2020).

6. Mistry, A., Usseglio-Viretta, F. L. E., Colclasure, A., Smith, K. & Mukherjee, P. P. Fingerprinting redox heterogeneity in electrodes during extreme fast charging. *J. Electrochem. Soc.* **167**, 90542 (2020).
7. Lim, J. et al. Origin and hysteresis of lithium compositional spatiodynamics within battery primary particles. *Science* **353**, 566–571 (2016).
8. Andrews, J. L. et al. Curvature-induced modification of mechano-electrochemical coupling and nucleation kinetics in a cathode material. *Matter* **3**, 1754–1773 (2020).
9. Fraggedakis, D. et al. A scaling law to determine phase morphologies during ion intercalation. *Energy Environ. Sci.* **13**, 2142–2152 (2020).
10. Zheng, H. et al. Quantitative characterization of the surface evolution for $LiNi_{0.5}Co_{0.2}Mn_{0.3}O_2$/graphite cell during long-term cycling. *ACS Appl. Mater. Interfaces* **9**, 12445–12452 (2017).
11. Bazak, J. D., Allen, J. P., Krachkovskiy, S. A. & Goward, G. R. Mapping of lithium-ion battery electrolyte transport properties and limiting currents with in situ MRI. *J. Electrochem. Soc.* **167**, 140518 (2020).
12. Siu, C. et al. Enhanced high-rate performance of nanosized single crystal ε-VOPO$_4$ with niobium substitution for lithium-ion batteries. *J. Electrochem. Soc.* **168**, 060519 (2021).
13. Wong, A. A., Rubinstein, S. M. & Aziz, M. J. Direct visualization of electrochemical reactions and heterogeneous transport within porous electrodes in operando by fluorescence microscopy. *Cell Rep. Phys. Sci.* **2**, 100388 (2021).
14. Steinrück, H.-G. et al. Concentration and velocity profiles in a polymeric lithium-ion battery electrolyte. *Energy Environ. Sci.* **13**, 4312–4321 (2020).
15. Zhao, Y. et al. A review on modeling of electro-chemo-mechanics in lithium-ion batteries. *J. Power Sources* **413**, 259–283 (2019).
16. McDowell, M. T., Cortes, F. J. Q., Thenuwara, A. C. & Lewis, J. A. Toward high-capacity battery anode materials: chemistry and mechanics intertwined. *Chem. Mater.* **32**, 8755–8771 (2020).
17. Heenan, T. M. M. et al. Identifying the origins of microstructural defects such as cracking within Ni-rich NMC811 cathode particles for lithium-ion batteries. *Adv. Energy Mater.* **10**, 2002655 (2020).
18. Ferraro, M. E., Trembacki, B. L., Brunini, V. E., Noble, D. R. & Roberts, S. A. Electrode mesoscale as a collection of particles: coupled electrochemical and mechanical analysis of NMC cathodes. *J. Electrochem. Soc.* **167**, 13543 (2020).
19. Whittingham, M. S. Lithium batteries and cathode materials. *Chem. Rev.* **104**, 4271–4301 (2004).
20. Yu, Y.-S. et al. Three-dimensional localization of nanoscale battery reactions using soft X-ray tomography. *Nat. Commun.* **9**, 921 (2018).
21. De Jesus, L. R., Andrews, J. L., Parija, A. & Banerjee, S. Defining diffusion pathways in intercalation cathode materials: some lessons from V$_2$O$_5$ on directing cation traffic. *ACS Energy Lett.* **3**, 915–931 (2018).
22. Santos, D. A. et al. Bending good beats breaking bad: phase separation patterns in individual cathode particles upon lithiation and delithiation. *Mater. Horiz.* **7**, 3275–3290 (2020).
23. Yao, K. P. C., Okasinski, J. S., Kalaga, K., Almer, J. D. & Abraham, D. P. Operando quantification of (de)lithiation behavior of silicon–graphite blended electrodes for lithium-ion batteries. *Adv. Energy Mater.* **9**, 1803380 (2019).
24. Yao, K. P. C., Okasinski, J. S., Kalaga, K., Shkrob, I. A. & Abraham, D. P. Quantifying lithium concentration gradients in the graphite electrode of Li-ion cells using operando energy dispersive X-ray diffraction. *Energy Environ. Sci.* **12**, 656–665 (2019).
25. Bai, Y., Zhao, K., Liu, Y., Stein, P. & Xu, B.-X. A chemo-mechanical grain boundary model and its application to understand the damage of Li-ion battery materials. *Scr. Mater.* **183**, 45–49 (2020).
26. Luo, Y. et al. Roadblocks in cation diffusion pathways: implications of phase boundaries for Li-ion diffusivity in an intercalation cathode material. *ACS Appl. Mater. Interfaces* **10**, acsami.8b10604 (2018).
27. Pan, A., Wu, H. Bin., Yu, L., & Lou, X. W. Template-free synthesis of VO$_2$ hollow microspheres with various interiors and their conversion into V$_2$O$_5$ for lithium-ion batteries. *Angew. Chem. Int. Ed. Engl.* **52**, 2226–2230 (2013).
28. Hu, Y.-S. et al. Synthesis and electrode performance of nanostructured V$_2$O$_5$ by using a carbon tube-in-tube as a nanoreactor and an efficient mixed-conducting network. *Angew. Chem. Int. Ed. Engl.* **48**, 210–214 (2009).
29. Horrocks, G. A., Likely, M. F., Velazquez, J. M. & Banerjee, S. Finite size effects on the structural progression induced by lithiation of V$_2$O$_5$: a combined diffraction and Raman spectroscopy study. *J. Mater. Chem. A* **1**, 15265–15277 (2013).
30. Rozier, P. et al. ε-Li$_x$V$_2$O$_5$ bronzes ($0.33 \leq x \leq 0.64$) a joint study by X-ray powder diffraction and ^{6}Li, ^{7}Li MAS NMR. *Eur. J. Solid State Inorg. Chem.* **33**, 1–13 (1996).
31. Murphy, D. W., Christian, P. A., DiSalvo, F. J. & Waszczak, J. V. Lithium incorporation by vanadium pentoxide. *Inorg. Chem.* **18**, 2800–2803 (1979).
32. Cocciantelli, J. M. et al. On the $\delta \rightarrow \gamma$ irreversible transformation in Li//V$_2$O$_5$ secondary batteries. *Solid State Ion.* **78**, 143–150 (1995).
33. Meulenkamp, E. A., Van Klinken, W. & Schlatmann, A. R. In-situ X-ray diffraction of Li intercalation in sol-gel V$_2$O$_5$ films. *Solid State Ion.* **126**, 235–244 (1999).
34. Li, Y. et al. Fluid-enhanced surface diffusion controls intraparticle phase transformations. *Nat. Mater.* **17**, 915–922 (2018).
35. De Jesus, L. R. et al. Lithiation across interconnected V$_2$O$_5$ nanoparticle networks. *J. Mater. Chem. A* **5**, 20141–20152 (2017).
36. Danner, T. et al. Thick electrodes for Li-ion batteries: a model based analysis. *J. Power Sources* **334**, 191–201 (2016).
37. Mistry, A. N. & Mukherjee, P. P. Probing spatial coupling of resistive modes in porous intercalation electrodes through impedance spectroscopy. *Phys. Chem. Chem. Phys.* **21**, 3805–3813 (2019).
38. Gao, H. et al. Revealing the rate-limiting Li-ion diffusion pathway in ultrathick electrodes for Li-ion batteries. *J. Phys. Chem. Lett.* **9**, 5100–5104 (2018).
39. Mistry, A. N., Smith, K. & Mukherjee, P. P. Electrochemistry coupled mesoscale complexations in electrodes lead to thermo-electrochemical extremes. *ACS Appl. Mater. Interfaces* **10**, 28644–28655 (2018).
40. Pietsch, P., Ebner, M., Marone, F., Stampanoni, M. & Wood, V. Determining the uncertainty in microstructural parameters extracted from tomographic data. *Sustain. Energy Fuels* **2**, 598–605 (2018).
41. Ebner, M., Chung, D.-W., García, R. E. & Wood, V. Tortuosity anisotropy in lithium-ion battery electrodes. *Adv. Energy Mater.* **4**, 1301278 (2014).
42. Usseglio-Viretta, F. L. E. et al. Resolving the discrepancy in tortuosity factor estimation for Li-ion battery electrodes through micro-macro modeling and experiment. *J. Electrochem. Soc.* **165**, A3403–A3426 (2018).
43. Wang, W., Juarez-Robles, D. & Mukherjee, P. P. Electroanalytical quantification of electrolyte transport resistance in porous electrodes. *J. Electrochem. Soc.* **167**, 80510 (2020).

Methods

Materials. Bulk V_2O_5 (99.2%) was purchased from Alfa Aesar. Ammonium vanadate (≥99.0%), ethylene glycol (anhydrous, 99.8%) and hydrazine (anhydrous, 98%) were purchased from Sigma-Aldrich. Aluminium foil for the battery cathode substrate with a thickness of 15 μm, polyvinylidene fluoride (PVDF, ≥99.5%), N-methyl-2-pyrrolidone (NMP), Celgard 2500 and SUPER-C45 conductive carbon black were purchased from MTI Corporation. The Li metal (99.9% trace metals basis) with a thickness of 0.75 mm and $LiPF_6$ electrolyte (1 M $LiPF_6$ in a 1:1 (v/v) mixture of ethylene carbonate (EC) and diethyl carbonate (DEC), battery grade) were bought from Sigma-Aldrich.

Sample characterization. SEM imaging was performed using a JOEL JSM-7500F FE-SEM instrument at an accelerating voltage of 5 kV with approximately 2.2 nm resolution. High-resolution TEM images were acquired using an FEI Tecnai G2 F20 ST instrument with 0.24 nm point resolution.

Laboratory X-ray diffraction. Powder X-ray diffraction data of bulk and NS V_2O_5 samples were obtained in Bragg–Brentano geometry on a short-arm Bruker D8-Focus diffractometer (Cu Kα, $\lambda = 1.5418$ Å source, 40 kV voltage, 25 mA current) equipped with a Lynxeye detector.

Laboratory electrochemical measurements. The electrochemical properties of bulk and NS V_2O_5 were tested in coin cells with metallic lithium as the anode and Celgard 2500 as separator. The coin cells were assembled in an argon-filled glovebox. For the laboratory electrochemical tests, each measurement was conducted multiple times on coin cells. The cathodes were fabricated by mixing V_2O_5, SUPER-C45 conductive carbon black and PVDF at a weight ratio of 70:20:10 in NMP solvent. The resulting mixture was then uniformly spread on an aluminium foil current collector, followed by drying at 70 °C overnight. The electrolyte solution was 1 M $LiPF_6$ in a 1:1 (v/v) mixture of EC and DEC. The cells were galvanostatically discharged/charged using a LAND battery cycler at room temperature. CV measurements were carried out using a BioLogic potentiostat.

The galvanostatic discharge/charge measurements were conducted at a C rate of C/20 between 2.8 and 4.0 V for three cycles, as shown in Fig. 1b,e. The cycling performance was examined at a C rate of C/2 between 2.8 and 4.0 V for 100 cycles, as shown in Fig. 1h.

MOS measurement. A slurry was prepared by mixing active material, SUPER-C45 conductive carbon black and PVDF at a weight ratio of 70:20:10 in NMP. Next, the slurry was spread onto a stainless-steel substrate by spin coating at a speed of 1,000 r.p.m. using a spin coater (Specialty Coating Systems, Spincoat G3P-8). Real-time stress measurements were performed using a MOS (k-Space Associates) to monitor substrate curvature variations. Briefly, the MOS measurement detects a change in curvature of the back of the electrode substrate. The MOS system uses a parallel array of laser beams that reflects off the sample surface and are captured on a CCD camera. The relative change between the detected laser position and reference laser position was utilized to calculate the curvature differential. The stress variation was deduced from Stoney's equation:[44,45]

$$\Delta\sigma = \frac{E_s h_s^2}{6 h_f (1 - \nu_s)} \Delta K \tag{1}$$

where $\Delta\sigma$ is the stress variation; E_s, h_s and ν_s are the Young's modulus, thickness and Poisson's ratio of the substrate, respectively; h_f is the thickness of the electrode; and ΔK is the change in the curvature of the substrate. Simultaneous detection of the laser array makes the operando stress measurement with cell cycling achievable by using a two-electrode electrochemical test cell with a quartz viewing window (MTI Corporation). A PARSTAT MC Multichannel potentiostat was used for electrochemical cycling. The set-up was placed on a vibration isolation table during cycling.

Operando X-ray diffraction measurements. *Operando electrochemical measurement.* Electrodes for operando studies were constructed by mixing carbon black (Vulcan XC-72, Cabot Corporation), graphite (300 mesh, 99%, Alfa Aesar), polytetrafluoroethylene (PTFE) binder (Sigma-Aldrich) and as-prepared V_2O_5 in a weight ratio of 7.5:7.5:15:70 using a mortar and pestle. The resulting mixture was pressed into a 9 mm diameter pellet and used as the working electrode. Lithium metal (Sigma-Aldrich) and glass fibre were used as the reference electrode and separator, respectively. The electrolyte was a 1 M $LiPF_6$ solution in a 1:1 (v/v) mixture of EC and DEC. During the measurements, the AMPIX cells and coin cells were cycled through discharge/charge at a C rate of C/20.

Operando synchrotron X-ray diffraction. The AMPIX cell, which models a coin-cell configuration, was assembled and equipped with X-ray transmissive windows for operando studies as described in previous work[46]. Kapton tape protected the glassy carbon window from Li exposure. Operando X-ray diffraction was performed in transmission mode at beamline 17-BM-B of the Advanced Photon Source (APS) of Argonne National Laboratory with an X-ray wavelength of 0.24117 Å. Multiple samples were analysed in parallel using the AMPIX multicell holder[46].

A diffraction pattern was acquired for each sample every 10 min with a collection time of 10 s using a PerkinElmer a-Si Flat Panel PEI 1621 detector. Modified coin cells commonly used for operando experiments use Kapton in X-ray-transparent windows, and indeed Kapton is permeable to air and moisture; air-sensitive battery components, such as Li metal, visibly change over the span of a few days. In contrast, AMPIX cells utilize relatively thick (0.5 mm) glassy carbon windows. This material is conductive, rigid and is not permeable by moisture and air. Utilization of carbon windows and fluorosilicate rubber seals ensures reliable and stable performance over a span of several months[47].

We have further taken great care to avoid artefacts induced as a result of beam damage. Factors that increase the probability of radiation damage include X-ray beam energy, high flux and extended exposure. Typically, the lower the X-ray energy, or the closer to the absorption edge of the elements within the electrodes, the higher the probability for damage. Specifically, we have used a high X-ray energy of 51 keV at beamline 17-BM and X-ray energies ranging from 60 to 150 keV, which are far above the V absorption edge[48] and considerably high enough to avoid beam-induced electrolyte decomposition[49]. Additionally, bending magnet beamlines have a relatively low flux compared with insertion device beamlines. An unfocused beam was used to minimize flux-related beam damage. The most prominent manifestation of beam damage is offset of phase transitions when compared to recorded electrochemistry (or lack of changes despite clear plateaus presented in the electrochemistry). In transmission experiments the observed state should be very closely correlated with the observed electrochemistry of the cell. In depth-profiling experiments, the middle of the electrode thickness (or the average of all states observed from the reaction front) should correlate with electrochemical features. As the data collected at 17-BM and 6-BM are consistent both with each other and with laboratory electrochemical results (Supplementary Fig. 16), we conclude that the results are not contaminated by degradation artefacts.

Datasets were analysed with GSAS II, an open source crystallography package[50]. Two-dimensional images were masked and integrated using LaB_6 as a standard for calibration. Background scans were performed on cells with the anode, electrolyte and separator, but without a cathode. Rietveld refinements were performed on select one-dimensional diffraction data to evaluate the lattice parameters on the basis of structural models from the Inorganic Crystal Structural Database.

Operando energy dispersive X-ray diffraction. Energy dispersive XRD data were obtained on CR2032 coin cells at the 6-BM-A beamline of Argonne's Advanced Photon Source. The EDXRD technique uses a multiwavelength 'white beam' of X-rays diffracted by the sample under study to produce the diffraction pattern. The use of EDXRD is advantageous over angle-resolved measurements as the high-energy white beam is able to penetrate battery housing materials, including steel, enabling operando diffraction measurements to be acquired across different sections of the 3D electrode. The white beam (60–150 keV) readily penetrates the stainless-steel casing. The intersection of the incident beam and the line-of-sight of the detector defines a probe volume located within the cell. A Ge point-detector placed 2.29° in the vertical plane (with respect to the incident beam) was used to measure the diffraction patterns of the working electrode at a rate of 40 s per spectrum. The incident beam height in the vertical plane was confined to fit the probe volume within the 30 μm thickness of the electrode pellets.

Phase-field model. The geometric microstructure was then meshed by Gmsh, where two distinct STL files have been exported from the GeoDict to define the geometry information for the active material phase and the electrolyte phase. The tetra-4 mesh was then generated for each phase. Next, the three-node triangle linear mesh was used to designate the interface between these two phases. Subsequently, using surface integration, the chemical reaction for lithium insertion and extraction during the charge/discharge process can be applied at the interface. To eliminate the rigid body motion, the three surfaces of the cube are fixed, for example, $u_x = 0$ at the $x = x_{min}$ surface, $u_y = 0$ at the $y = y_{min}$ surface and $u_z = 0$ at the $z = z_{min}$ surface.

The free energy density for this chemomechanically coupled process is introduced as follows[51]:

$$\psi = \psi^c + \psi^i + \psi^e \tag{2}$$

where ψ^c, ψ^i and ψ^e denote the bulk chemical free energy density, the energy penalty at the interface and the elastic energy density, respectively. They are assumed to have the following form:

$$\psi^c = RTC_{max}\left[c\ln c + (1 - c)\ln(1 - c) + \chi c(1 - c)\right] \tag{3}$$

$$\psi^i = \frac{1}{2}C_{max}\kappa\left|\nabla c\right|^2 \tag{4}$$

$$\psi^e = \frac{1}{2}\varepsilon_{kl}^e : C_{ijkl} : \varepsilon_{ij}^e = \frac{1}{2}(\varepsilon_{ij} - \varepsilon_{ij}^c) : C_{ijkl} : (\varepsilon_{kl} - \varepsilon_{kl}^c) \tag{5}$$

where c is the normalized concentration, R and T denote the gas constant and temperature, respectively, and C_{max} is the maximum stoichiometric fraction of

lithium in $Li_xV_2O_5$. Here, χ is a coefficient representing the interaction between two phases, κ represents the coefficient of the gradient penalty term and is associated with the interfacial energy. C_{ijkl} and ε_{ij}^e represent the stiffness tensor and the elastic strain tensor, respectively. Note that the elastic strain is defined as the total strain tensor ε_{ij} subtracted by the chemical strain ε_{ij}^c, which takes the form of $\varepsilon_{ij}^c = \frac{1}{3}\Omega c\delta_{ij}$ in the isotropic case, with Ω being the partial molar volume.

Therefore, the chemical potentials and the stress can be listed as below:

$$\mu^c = \frac{\partial \psi^c}{\partial c} = RT\left[\ln c - \ln(1-c) + \chi(1-2c)\right] \qquad (6)$$

$$\mu^i = \frac{\delta \psi^i}{\delta c} = -\kappa\Delta c \qquad (7)$$

$$\mu^e = \frac{\partial \psi^e}{\partial c} = -\Omega\sigma_h \qquad (8)$$

$$\sigma_{ij} = \frac{\partial \psi^e}{\partial \varepsilon_{ij}} = C_{ijkl}\varepsilon_{kl}^e = C_{ijkl}(\varepsilon_{kl} - \varepsilon_{kl}^e) \qquad (9)$$

where σ_{ij} (or in tensor notation σ) is the stress tensor and $\sigma_h = \frac{1}{3}(\sigma_{11} + \sigma_{22} + \sigma_{33})$ is the hydrostatic stress.

As such, the linear moment balance and the mass conservation of lithium inside the nanosphere particle and the bulk can be expressed as:

$$\nabla\sigma = 0 \qquad (10)$$

$$\frac{\partial c}{\partial t} = \nabla(M\nabla\mu) \qquad (11)$$

$$\mu = \mu^c + \mu^i + \mu^e \qquad (12)$$

where $M = Dc(1-c)$ is the mobility term, with D the diffusivity of lithium in V_2O_5. The related boundary conditions are:

$$u = u_0 \text{ on } \Gamma_u \qquad (13)$$

$$-M\nabla\mu \cdot n = J_0 \text{ on } \Gamma_j \qquad (14)$$

where u_0 is the prescribed displacement on boundary Γ_u and J_0 is the applied flux for the lithiation process. In our simulation, a $\frac{C}{20}$ rate is applied for the galvanostatic discharge process.

In the phase-field simulation, two different representative volume elements (RVEs) were used. The cubic size of the NS-type RVE was 250 nm × 250 nm × 250 nm, where small spherical particles with a diameter of 60 nm fill the RVE cubic. The bulk-type RVE has a cubic size of 4 μm × 4 μm × 4 μm, with the RVE being packed with small ortho bricks measuring 1.2 μm × 0.7 μm × 0.3 μm. The electrolyte was represented by the pore phase (or the empty space) in both situations, thereby, the chemical reaction takes place at the interface between the electrolyte and the active material. Meanwhile, to eliminate the rigid body motion, the symmetric displacement restriction was applied to both cases, namely $u_x = 0$, $u_y = 0$ and $u_z = 0$ were applied at the $x = 0$, $y = 0$ and $z = 0$ surfaces.

Mesoscale model. The calculation of particle-scale diffusion timescale was as follows:

$$t_s = l_{particle}^2/D_s \qquad (15)$$

Here $l_{particle}$ is an appropriate intercalation length for the particles (the radius for spherical and thickness for the platelet particles) and $D_s \approx 5 \times 10^{-15} \text{ m}^2\text{s}^{-1}$ is a representative diffusivity for lithium intercalation in V_2O_5 (ref. [26]).

The calculation of the diffusion timescale in the electrolyte pore network is as given by:

$$t_e \approx L_{electrode}^2/\frac{\varepsilon}{\tau}D_e \qquad (16)$$

where $L_{electrode}$ is electrode thickness, ε is porosity, τ is tortuosity and D_e is salt diffusivity in the electrolyte. For the electrode used here (1 M $LiPF_6$ in EC:DEC), $D_e \approx 2 \times 10^{-10} \text{ m}^2\text{s}^{-1}$, as measured elsewhere [52] (see 'specifications of porous V_2O_5 electrode' in Supplementary Table 10.)

The driving force for intercalation reaction at the particle–electrolyte interface is the overpotential, η:

$$\eta = \phi_s - \phi_e - U(x) \qquad (17)$$

where ϕ_s is the potential of active materials (spatially uniform given high carbon and binder contents)[39,53], ϕ_e is local electrolyte potential (varies in response to local ionic concentration) and U is the thermodynamic potential (varies with degree of intercalation as shown in Fig. 6a). The thermodynamic potential is the equilibrium material characteristic, whereas ϕ_s and ϕ_e identify departures from equilibrium. If the electrolyte concentration gradients are minimal, ϕ_e is nearly uniform and leads to an almost similar local overpotential, η, driving intercalation. Accordingly, one would observe small differences in the intercalation response of particles at different spatial locations (Fig. 6c). On the other hand, when electrolyte transport is hindered, ϕ_e distributes to cause preferential intercalation/deintercalation of active particles close to the separator. Accordingly, one observes intercalation gradients along the electrode thickness, as shown in Fig. 6b. Such gradients are more pronounced in the two-phase regions since $U(x)$ is almost constant and accordingly the intercalation preference, that is, distribution of overpotentials, η, depends more strongly on electrolyte potential, ϕ_e. This also accounts for the greater total overpotential in two-phase regions as seen in Fig. 6a. The total overpotential is the difference between voltage and the thermodynamic potential at the same intercalation state and is more apparent in the inset figures in Fig. 6a.

When the intercalation is stopped at 2.8 V and deintercalation is initiated, the pre-existing stoichiometric gradients do not have time to relax and this compounds the stoichiometric polarization. Hence, the electrode with micrometre-sized V_2O_5 platelets exhibits a larger capacity difference, δQ, of 0.8% compared with 0.1% for the electrode with spherical NS V_2O_5. Here, the capacity difference is computed as:

$$\delta Q = \left(Q_{intercalation}^{1st} - Q_{deintercalation}^{1st}\right)/Q_{intercalation}^{1st} \qquad (18)$$

FIB-SEM tomography. Electrodes of bulk and NS V_2O_5 were prepared by mixing V_2O_5, SUPER-C45 conductive carbon black and PVDF at a weight ratio of 70:20:10 in NMP. The resulting mixture was then uniformly spread on an aluminium foil current collector, followed by drying at 70 °C overnight. These electrodes were same as the electrodes used for electrochemical measurements.

Three-dimensional slice and view images were acquired using an FEI Helios G4 CX Dualbeam system with the Auto Slice and View software. A step size of 50 nm was selected, and approximately 200 images of the cross-sections were taken for each dataset. 3D models were then reconstructed on the basis of the above data with the Avizo software. For the detailed 3D slice and view procedure, the electron beam was used for imaging each section, and the ion beam was used for serial sectioning. First, an ~1 μm thick platinum (Pt) layer was deposited on top of the film to protect the region of interest (ROI) from ion-beam damage. Next, trenches surrounding the ROI were created to reveal the cross-sections of the film. A fiducial mark was then made near the ROI to enable automatic alignment of the electron and ion beams. In this experiment, a step size of 50 nm was selected, and over 200 images of the cross-sections were taken for each sample (10 μm in depth) (see 'FIB-SEM images of V_2O_5 electrode' in Supplementary Fig. 17).

EIS measurement. Composite electrodes of bulk and NS V_2O_5 samples were used in a symmetric coin-cell assembly (CR2032). Bulk (thickness = 7.51 μm) and NS (thickness = 15.91 μm) electrodes were both punched to a diameter of 1.27 cm. A blocking electrolyte (non-intercalating), $TBAClO_4$ (10 mM), in EC:dimethyl carbonate) (1:4 wt%), was used between two electrodes of identical composition to perform EIS measurements, under open-circuit voltage at BioLogic system in the frequency range of 1 MHz to 10 mHz.

Simplified-generalized transmission line model. EIS analysis provides the total impedance of the cell (Z_{cell}) consisting of a high-frequency bulk electrolyte and experimental set-up resistance (R_{HFR}), contact impedances between the electrode and current collector (Z_{cont}) and internal impedances of porous electrodes (Z_{el}). The Bode plots of V_2O_5 electrodes are presented in Supplementary Fig. 18.

The real part of the Z_{cell} is given by

$$R_{cell} = R_{HFR} + R_{cont} + K \times R_{ion} \qquad (19)$$

where K is the characteristic coefficient and R_{ion} is the electrolyte transport resistance. R_{ion} is the most important parameter here, as it provides an estimation of the tortuosity. To obtain a reasonable estimate of R_{ion}, the measured impedance was fitted with the simplified-generalized transmission line model (S-GTLM) using a MATLAB script named 'fminsearch' following the procedures from ref. [43].

Then, the tortuosity value can be obtained from R_{ion}, as given in ref. [54]:

$$\tau = \frac{R_{ion}A\kappa\varepsilon}{2d} \qquad (20)$$

where A is the cross-sectional area of the electrode, d is the thickness of the electrode, ε is the porosity of the electrode and κ is the conductivity of the electrolyte. The factor of 2 in the denominator is due to the use of two symmetric cells, as the impedance of two identical electrodes is measured.

NS V_2O_5 synthesis. NS V_2O_5 was synthesized by a sol–gel process to stabilize VO_x nanocrystals, followed by high-temperature oxidation. First, 0.5 g of ammonium

vanadate was dissolved into 10 ml of deionized water ($\rho = 18.2\,M\Omega\,cm^{-1}$) at 80–85 °C using a round-bottomed flask placed over an oil bath under magnetic stirring. Next, 5 ml ethylene glycol was added to the transparent light-yellow solution. Subsequently, 0.7 ml of a 4.7 wt% aqueous hydrazine solution was added to the solution and was allowed to react for 30 min. The obtained black suspension was dispersed in 250 ml acetone. The precipitate centrifuged at 8,000 r.p.m. was discarded. The precipitate centrifuged at 12,000 r.p.m. was collected, dried at 80 °C overnight in an oven under static air and annealed at 250 °C for 24 h.

Data availability

The data that support the findings of this study are available within the paper and its Supplementary Information. Source data are provided with this paper. Any other data are available from the corresponding author on reasonable request.

Code availability

All original code scripts have been provided and are freely available.

References

44. Stoney, G. G. The tension of metallic films deposited by electrolysis. *Proc. R. Soc. Lond. A* **82**, 172–175 (1909).
45. Nix, W. D. Mechanical properties of thin films. *Metall. Trans. A* **20**, 2217 (1989).
46. Borkiewicz, O. J. et al. The AMPIX electrochemical cell: a versatile apparatus for *in situ* X-ray scattering and spectroscopic measurements. *J. Appl. Crystallogr.* **45**, 1261–1269 (2012).
47. Liu, H. et al. Intergranular cracking as a major cause of long-term capacity fading of layered cathodes. *Nano Lett.* **17**, 3452–3457 (2017).
48. Horrocks, G. A. ; et al. Vanadium K-edge X-ray absorption spectroscopy as a probe of the heterogeneous lithiation of V_2O_5: first-principles modeling and principal component analysis. *J. Phys. Chem. C* **120**, 23922–23932 (2016).
49. Borkiewicz, O. J., Wiaderek, K. M., Chupas, P. J. & Chapman, K. W. Best practices for operando battery experiments: influences of X-ray experiment design on observed electrochemical reactivity. *J. Phys. Chem. Lett.* **6**, 2081–2085 (2015).
50. Toby, B. H. & Von Dreele, R. B. GSAS-II: the genesis of a modern open-source all purpose crystallography software package. *J. Appl. Crystallogr.* **46**, 544–549 (2013).
51. Stein, P. & Xu, B. 3D isogeometric analysis of intercalation-induced stresses in Li-ion battery electrode particles. *Comput. Methods Appl. Mech. Eng.* **268**, 225–244 (2014).
52. Lundgren, H., Behm, M. & Lindbergh, G. Electrochemical characterization and temperature dependency of mass-transport properties of $LiPF_6$ in EC:DEC. *J. Electrochem. Soc.* **162**, A413–A420 (2014).
53. Mistry, A. N., Smith, K. & Mukherjee, P. P. Secondary-phase stochastics in lithium-ion battery electrodes. *ACS Appl. Mater. Interfaces* **10**, 6317–6326 (2018).
54. Landesfeind, J., Hattendorff, J., Ehrl, A., Wall, W. A. & Gasteiger, H. A. Tortuosity determination of battery electrodes and separators by impedance spectroscopy. *J. Electrochem. Soc.* **163**, A1373 (2016).

Author contributions

Y.L., B.-X.X. and S.B. designed the project. Y.L. performed material synthesis, microscopy experiments, operando X-ray diffraction and EDXRD experiments and data analysis. A.M. designed the mesoscale model. B.-X.X., Y.B. and S.R. contributed to the phase-field simulations. Y.Z. performed MOS experiment and data analysis. K.X., Y.Z. and D.Z. conducted FIB-SEM experiment and 3D reconstruction. S.S. performed EIS fitting and calculated tortuosity. J.V.H. helped with operando X-ray diffraction and EDXRD experiments. A.C.C. helped with operando energy dispersive X-ray diffraction data analysis. L.C. performed TEM measurements. K.W. helped with battery assembly. M.P., P.P.M., B.-X.X. and S.B. supervised the whole project. All authors contributed to writing and editing the manuscript.

Competing interests

The authors declare no competing interests.

Additional information

Supplementary information The online version contains supplementary material available at https://doi.org/10.1038/s41563-021-01151-8.

Correspondence and requests for materials should be addressed to Partha P. Mukherjee, Bai-Xiang Xu or Sarbajit Banerjee.

Peer review information *Nature Materials* thanks Thomas Heenan and Louis Piper for their contribution to the peer review of this work.

Reprints and permissions information is available at www.nature.com/reprints.